Journal of Power Sources 196 (2011) 9989–9997

Contents lists available at ScienceDirect

Journal of Power Sources

journal homepage: www.elsevier.com/locate/jpowsour

Effect of Ni content in SOFC Ni-YSZ cermets: A three-dimensional study by FIB-SEM tomography

N. Vivet[a], S. Chupin[a], E. Estrade[a], A. Richard[b], S. Bonnamy[c], D. Rochais[a], E. Bruneton[a,*]

[a] CEA-Le Ripault, BP 12, 37260 Monts, France
[b] Centre de Microscopie Electronique, Université d'Orléans, rue de Chartres, BP 6759, 45067 Orléans Cedex 2, France
[c] Centre de Recherche sur la Matière Divisée, 1b rue de la Férollerie, 45071 Orléans Cedex 2, France

ARTICLE INFO

Article history:
Received 8 April 2011
Received in revised form 10 June 2011
Accepted 5 July 2011
Available online 12 July 2011

Keywords:
FIB
Tomography
SOFC
Percolation threshold
Tortuosity
Effective properties

ABSTRACT

SOFC anodic cermets with varying Ni concentrations have been studied in terms of electric percolation and electrochemical activity. Serial sectioning using focused ion beam-scanning electron microscopy (FIB-SEM) has been implemented to reconstruct the three-dimensional microstructure. A Passive Voltage Contrast technique has also been used to evaluate the degree of percolation of the electrically conducting phase (Ni) in the Ni-YSZ cermets. Volumetric ratios, connectivity of the phases and effective electrical conductivity have been estimated to establish a relation between the volumetric ratio of Ni and the electrical conductivity. These results were then correlated with experimental measurements. From the 3D reconstructions, interface features (interface and surface areas, three-phase boundary length: TPB_L) and ionic effective conductivities have been compared, enabling a characterization of the electrochemical activity of the samples. After reduction of the initial NiO, 40:60 vol.% Ni:YSZ appeared to be the optimal composition, providing an anode with high electronic conductivity and the largest active TPB_L.

1. Introduction

A solid-oxide fuel cell (SOFC) is an all-solid device that produces electricity directly by oxidizing a fuel. It represents a potential breakthrough technology for a low-cost, clean and highly efficient production of electricity and heat [1]. Redox reactions occur in the internal SOFC electrodes that are composed of porous materials. Consequently, the microstructure of the electrode is likely to affect the electrochemical activity of an SOFC electrode. Advanced fuel-cell electrodes typically have complex internal microstructures that provide the necessary conditions for gas diffusion and electrochemical reactions.

Ni-yttria stabilized zirconia (Ni-YSZ) cermets have found extensive use as SOFC anodes due to their high electrochemical catalytic activity towards hydrogen oxidation, high electrical conductivity and chemical stability. Moreover, Ni-YSZ anodes present good thermo-mechanical and sintering compatibilities with many electrolyte materials, which are often YSZ. The Ni-YSZ cermets used for SOFC anodes usually have a volume fraction of solid Ni in the range 40–70% [2]. However, due to a large discrepancy of the thermal expansion coefficient (TEC) of Ni (TEC: $1.69 \times 10^{-5}\,K^{-1}$) and 8 mol% yttria stabilized zirconia (8YSZ) (TEC: $1.05 \times 10^{-5}\,K^{-1}$) [3], the Ni content is critical to the mechanical and microstructural stability of Ni-YSZ cermets. For example, the most predominant microstructural change facilitating the degradation of Ni-YSZ anodes is the agglomeration and coarsening of the Ni phase, which increases with a higher Ni content [4]. Consequently, if one could retain sufficient electrical conductivity at a reduced nickel content, this might lower the deleterious effects of thermal mismatch and coarsening of the Ni phase. However, reducing the solid Ni content to a volume fraction below 35–40% results in a non-percolating Ni network and therefore in a severely diminished electrical conductivity of Ni-YSZ anodes [5–7].

In a simple metal–insulator transition system, the Effective Medium Percolation Theory (EMPT) predicts that the electronic conductivity threshold occurs when the transition system has a metal concentration of 33.3 vol% [8]. The EMPT considers the overall conductivity of a random mixture of particles that display two different conductivities under the assumption that the inhomogeneous surrounding of a particle can be replaced by an effective medium. The percolation threshold value (33.3%) is then independent of the microstructure of the material. Even if the EMPT reproduces the electrical continuity/discontinuity transition, no general theory exists that perfectly matches the experimental

* Corresponding author. Tel.: +33 247344193; fax: +33 247345174.
E-mail address: eric.bruneton@cea.fr (E. Bruneton).

0378-7753/$ – see front matter © 2011 Elsevier B.V. All rights reserved.
doi:10.1016/j.jpowsour.2011.07.010

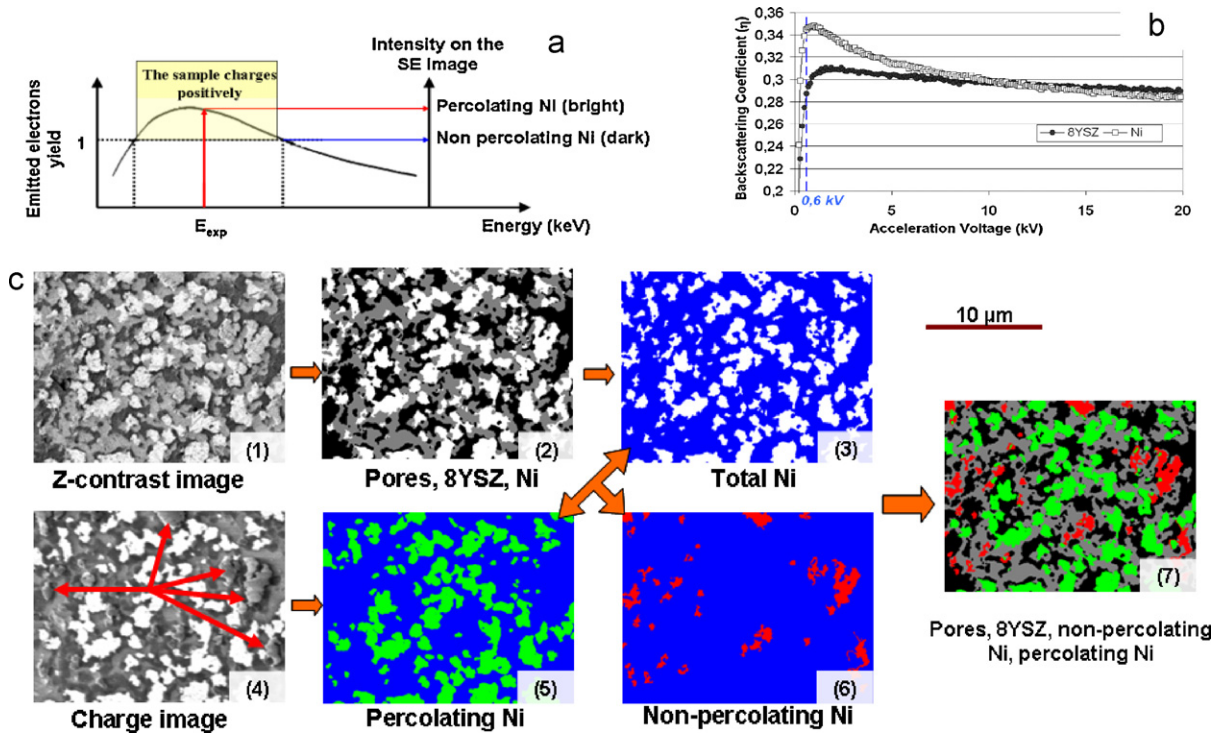

Fig. 1. (a) Schematic illustration of the charge contrast mechanism: For primary electron beam energy of E_{exp}, the conductive phases (percolating Ni) appear bright on the SE image while the insulated phases (non-percolating Ni) appear dark. (b) Illustration of the results from Monte Carlo calculations of backscatter coefficients for Ni and 8YSZ as a function of the acceleration voltage. (c) Analysis procedure of the PVC technique: the Z-contrast image (1) allows to separate pores, 8YSZ and Ni phases respectively in dark, grey and white in (2,3). The percolating Ni phase (in green in (5)) is extracted from the charge image (4), and the subtraction between (3) and (5) leads to the binary plane of the non-percolating phase (in red in (6)). The non-percolating Ni is also highlighted in (4) by red arrows. (7) Combines the segmented phases (2), (5) and (6) separating pores (black), 8YSZ (grey), percolating Ni (green) and non-percolating Ni (red). The scale bar is the same in the seven images and is displayed at the top of (7). (For interpretation of the references to color in this figure legend, the reader is referred to the web version of the article.)

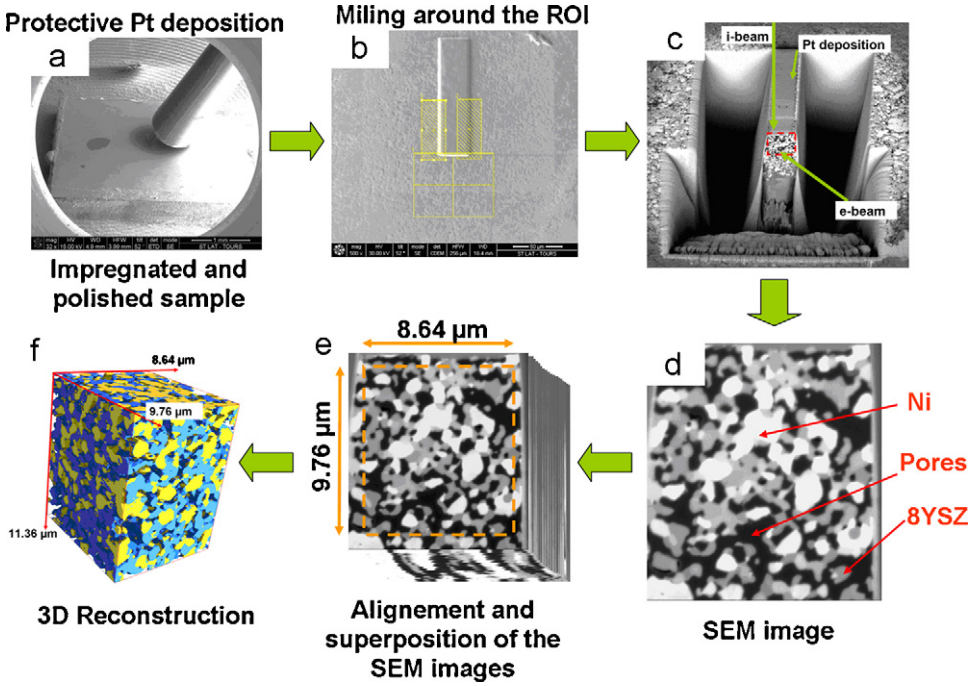

Fig. 2. Main steps of the 3D reconstruction using the FIB tomography technique: (a) Protective Pt deposition, (b and c) milling of a trench around the area of interest, (d) optimization of the SEM imaging parameters to obtain high contrast between the three phases, (e and f) successive milling and imaging steps, alignment and concatenation of the SEM images to obtain a 3D image.

percolation threshold since this is affected by several factors including the size of the starting powders, the size ratio of particles, the particle distribution, the porosity, and the pore size of the cermet [9].

Moreover, in order to provide a reliable value of the percolation threshold, the Ni volume fraction must be calculated accurately. Despite this, the Ni volume fractions have up until now either been deduced from the initial fabrication parameters, or estimated through SEM images. Since 2006, FIB-SEM tomography has appeared as a powerful technique to provide a 3D analysis of SOFC electrodes including the volumetric fraction and connectivity of each phase [10–23]. For example, in a previous paper [24], we described the optimization of the process for obtaining a high-quality 3D reconstruction of a Ni-YSZ anode using FIB-SEM tomography. Various microstructural parameters (volume fraction, connectivity of the phases), interfacial features (surface area and TPB_L), effective conductivities (thermal, electronic and ionic) and tortuosity of the solid phases have been estimated.

Thyden et al. have reported on a passive voltage contrast (PVC) technique to visualize the degree of percolation of the electrically conducting phase (Ni) in uncoated Ni-YSZ cermets by low voltage SEM [25]. This efficient technique provides a 2D visualization (image) of a 3D phenomenon (electrical conductivity). For this purpose, lateral and inlens secondary electron (SE) detectors of a field emission SEM with low acceleration voltage have been used. The analysis of the SEM images obtained by the two contrast techniques has led to the determination of the surface fraction of each component: pores/YSZ/percolating Ni/non-percolating Ni.

In the present study, both FIB-SEM tomography and PVC techniques have been used to compare five Ni-YSZ anodes with different volumetric Ni ratio. The real volumetric ratios and connectivities of the phases have been determined using a method described elsewhere [24]. The effective electrical conductivity has been estimated as a function of the Ni percolation. These results were then correlated with experimental measurements of the electrical conductivity providing relationships between microstructure and electrical performance. Interface features (interface and surface areas, TPB_L), tortuosity of the Ni phase, and effective ionic conductivities have also been compared as a function of the anode composition.

2. Experimental

2.1. Samples

The deposition of NiO–8YSZ anodes with three-layer coatings was performed by screen-printing onto circular zirconia supports using inks with optimized compositions. NiO from J.T. Baker (USA) and 8YSZ from Tosoh (Japan) were employed as raw materials to prepare the NiO–8YSZ at different Ni volume ratios. Technical data from suppliers and lab characterizations have already been given [24].

First of all, in order to prepare composite powders with different NiO ratios (i.e., 45, 51, 54, 56 and 61 wt.%), the raw materials were weighed and ball-milled in ethanol for 18 h. Next, the solvent was evaporated for 24 h at 90 °C. After cooling, and to prevent agglomerate formation, a 200 μm screening led to a NiO–8YSZ composite powder with the desired Ni ratio.

Anode inks were prepared by mixing NiO–8YSZ powder with alpha-terpiniol and Nextech ink as the solvent and the medium respectively and with alkyl ether phosphate acid as dispersant. Compositions of samples A1 through A5 are listed Table 1. After mixing and grinding the anode inks for 15 min, the ink was screen-printed onto circular zirconia supports through PET1000 screens. The first layer of the anode ink was dried in an oven for 20 min at 100 °C. A second and a third layer of the same anode composition were subsequently screen-printed onto the first layer. This experimental procedure was applied for each anode listed in Table 1. The electrodes were fired at 1300 °C for 3 h. The reduction treatment was performed at 800 °C for 4 h using a 2 °C min^{-1} ramp rate in Ar–H_2 (2 vol.%, 0.5 l min^{-1} for H_2).

Table 1
Anode composition and size of the five 3D reconstructed volumes.

Sample	A1	A2	A3	A4	A5
Composition: NiO wt.%	45	51	54	56	61
3D reconstruction size (μm)					
X	9.12	8.88	9.60	8.64	9.04
Y	6.56	9.92	7.68	9.76	9.44
Z	5.84	7.20	9.32	11.36	8.24

2.2. Passive voltage contrast (PVC) technique

The PVC technique is performed with a SEM at low voltage and renders it possible to detect phases with different electrical conductivities [25]. Indeed, if the primary electron beam energy is below approximately 2 kV, the number of emitted electrons (SE + backscattered electrons, BSE) may be larger than the number of primary electrons reaching the specimen (Fig. 1(a)). As a consequence, a net positive charge accumulates at the surface, and the lowest-energy SE emitted may be attracted back to the specimen because of the positive potential attraction. If a low voltage primary beam interacts with a non-conductive part of a sample, a positive charge without a path to the substrate accumulates on the specimen surface. Since the number of emitted electrons is lower than the incident ones, this part of the sample will appear darker than the conductive part (Fig. 1(a)). The contrast on the SEM images will be highly dependent on the conductive state. These "charge images" are better highlighted by an inlens detector located at a shorter distance from the sample than a conventional lateral detector [25].

In order to determine the fraction of each component (pores; 8YSZ; percolating Ni and non-percolating Ni), a "Z-contrast image" separating pores, 8YSZ and Ni was first acquired and then correlated to the corresponding "charge image". As illustrated in Fig. 1(b), the difference between the backscatter coefficients (η) of Ni and 8YSZ was at a maximum for an accelerating voltage smaller than 1 kV as shown by Monte Carlo calculations [26]. The difference in η can be detected by a backscatter detector (efficient at low voltage) or directly by a lateral SE detector leading to the "Z-contrast image".

The sample preparation is a key parameter for the quality of the SEM images. In order to easily distinguish the pores and to avoid mistakes due to the depth of field, the samples were infiltrated with an epoxy resin (EPOFIX, Struers) under vacuum and then polished. The samples were not coated with a conductive layer so as to allow the detection of the charge contrast. They were finally grounded to the sample stage in the microscope via a copper tape.

The microscope used in this work was a Hitachi S4500. A lateral SE detector was used to record the "Z-contrast image" (Fig. 1(c)) with: an acceleration voltage $V = 0.6$ kV, a working distance (WD) of 16 mm and a frame scan speed of 20 s by frame. To achieve the optimal contrast between percolating (bright) and non-percolating Ni (dark) areas (Fig. 1(c)), an inlens detector was utilized. The optimum acquisition conditions were determined as: $V = 0.6$ kV, $WD = 5$ mm and the scan speed: 20 s by frame. The previous two SEM images were then superimposed, aligned and submitted to a basic image segmentation (Avizo software [27]) in order to analyze the pores, 8YSZ, the conductive Ni and the non-conductive Ni.

Table 2
Volume fraction and percolation fraction deduced from the analysis of the 3D reconstructions. The standard deviation values were calculated from the variation in surface area in each slice in the three main directions (*X*, *Y*, *Z*). The percolation fraction of a phase was defined as the ratio of its percolated volume to its total volume.

Sample		A1			A2			A3			A4			A5		
Pore	Volume fraction (%)	35			36			39			41			48		
	Standard deviations (X,Y,Z)	4	4	2	3	3	3	3	3	3	2	2	4	3	3	5
	Pore percolation (%)	98.9			99.6			99.5			99.8			99.7		
8YSZ	Volume fraction (%)	50			48			35			33			22		
	Standard deviations (X,Y,Z)	4	6	4	5	4	5	5	4	3	2	4	5	3	3	3
	8YSZ percolation (%)	99.9			99.8			99.1			99.2			96.7		
Ni	Volume fraction (%)	15			16			26			26			30		
	Solid volume fraction (%)	23			25			43			44			58		
	Standard deviations (X,Y,Z)	3	5	3	3	2	3	6	5	4	3	3	5	3	5	4
	Ni percolation (%)	0			0			88.6			87.1			97.4		

Table 3
Electronic and ionic conductivities of pores, 8YSZ and Ni at 1123 K and RT.

	Pores	8YSZ	Ni
σ_{ionic} (10^{-3} S cm^{-1}) at 1123 K	0	14 [8]	10^{-5} [6]
$\sigma_{electronic}$ (S cm^{-1}) at 1123 K	0	10^{-6} [6]	10^{4} [6]
$\sigma_{electronic}$ (S cm^{-1}) at RT	0	6×10^{-3} [32]	1.5×10^{5} [32]

2.3. FIB tomography

A dual-beam FIB-SEM (FEI Strata DB 400-S) was utilized to obtain the 3D reconstructions of the 5 samples as previously described [24]. The samples were infiltrated with epoxy resin, thinned, glued onto a stub and finally metalized with a thick conducting gold layer. Then, a thick Pt layer was deposited to protect the region of interest (ROI) before wide and deep trenches were milled. As discussed in our previous work, a drift correction procedure was used to keep a constant interslice value. The acquisition data process is outlined in Fig. 2. Between 60 and 115 SEM images were, depending on the sample, recorded with a spacing of 100 nm between each slice. The sizes of the 3D reconstruction are given in Table 2. The datasets have been resampled to obtain 10 nm × 10 nm × 10 nm cubic voxels.

The volume fractions (i.e., the fraction of Ni, 8YSZ and pores with respect to these three phases) were estimated by using a voxel counting routine. The solid volume fractions of Ni and 8YSZ (i.e., the fraction of Ni and 8YSZ with respect to the solid Ni and 8YSZ phases) were defined as: $V_{Ni,sol} = V'_{Ni}/(V'_{Ni} + V'_{8YSZ})$ and $V_{YSZ,sol} = V'_{8YSZ}/(V'_{Ni} + V'_{8YSZ})$, for the Ni and 8YSZ phases, respectively, where the V' terms correspond to the measured volumes from 3D images analysis.

Voxels of the same nature in contact were regrouped to form clusters. A cluster was defined as "percolated" only if it was connected to the six boundary faces of the volume. The surface areas of each phase and the interface areas were estimated by counting the number of voxels that were in contact with at least one voxel of different nature. These values were then normalized to the sample volume to obtain the specific surface area (SSA) and specific interface area (SIA) values (in $\mu m^2\ \mu m^{-3}$).

Table 4
Surface area fraction of each phase deduced from the PVC analysis. The percolation fraction of the Ni phase was defined as the ratio of the percolated Ni surface area fraction to the total Ni surface area fraction.

Sample	A1	A2	A3	A4	A5
Pores (surface area, %)	33	33	37	40	42
8YSZ (surface area, %)	55	53	33	31	24
Ni (surface area, %)	12	14	30	29	34
Percolated Ni (surface area, %)	0	0	25	23	30
Non-percolating Ni (surface area, %)	12	14	5	6	4
Percolated Ni fraction (%)	0	0	83	79	88

The surface to volume ratio (SVR) of each phase was obtained by normalizing the surface area values by the phase volume. The TPB_L (in $\mu m\ \mu m^{-3}$) was estimated with the classical edge segment length technique with normalization to the sample volume. A TPB was defined as "active" when it belongs to percolating Ni, YSZ and porous phases. The effective electronic and ionic conductivities have been estimated by solving the diffusive transport equation [28–31]. Finally, the tortuosity of the Ni phase was deduced from these results. The calculation of the effective conductivities was carried out with the elemental conductivities obtained from literature and presented in Table 3.

3. Results

The above-mentioned characterization methods were applied to the five Ni-8YSZ cermets with different initial volumetric NiO ratios. The volume fraction and connectivity as well as the electrical conductivity were investigated first. Next, the SSA, the SIA, the SVR and the TPB_L were estimated. Finally, the effective ionic conductivity was calculated.

3.1. Volume fraction and connectivity of the phases

The five volumes reconstructed by FIB-SEM tomography are presented in Fig. 3(a). The corresponding phase ratios, taking into account either the three phases or only the solid ones, are listed in Table 2. As expected, from the sample A1 to the sample A5, the pore and the Ni fractions increased – due to NiO reduction – while that of 8YSZ decreased. Table 2 also suggests that even though the starting composition was somewhat different, the samples A1 and A2 as well as the samples A3 and A4 had comparable compositions.

The procedure for quantifying the connectivity described above (see Section 2.3) was applied for each phase (Table 2). Regardless of the sample, the percolated fraction was about 100% for the pores and 8YSZ, indicating that these phases were almost totally percolated. For the Ni phase, the percolated fraction was null for the samples A1 and A2 while it was very high for the other samples. Fig. 3(b) shows non-percolated Ni clusters in the samples A1 and A2 and quasi-completely percolated ones in the samples A3, A4 and A5.

The images acquired with the SE lateral detector provided a good separation between pores (darker contrast), 8YSZ (intermediate contrast) and Ni (brighter contrast) as observed in Fig. 1(c) for

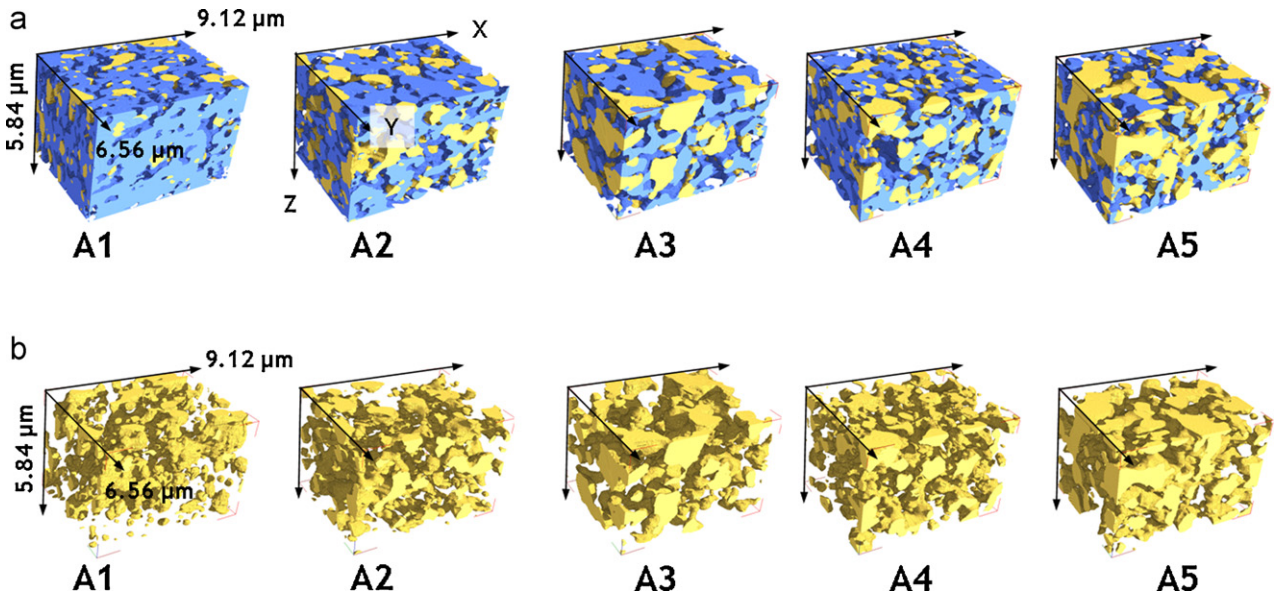

Fig. 3. (a) Reconstructed 3D anode microstructures (Ni: yellow, 8YSZ: blue, Pore: transparent). A common volume size was fixed allowing the comparison of the samples. (b) The corresponding Ni phase of each sample illustrates that Ni particles are not percolated in samples A1 and A2 while they are almost totally percolated in samples A3, A4 and A5. (For interpretation of the references to color in this figure legend, the reader is referred to the web version of the article.)

the sample A5. The calculated area fractions (Table 4 and Fig. 4(a)) did not exactly match the volume fractions calculated from the 3D FIB-SEM reconstructions (see Table 2). The standard deviation values associated with the volume fractions, obtained considering the fraction of the phases on each slice of the reconstructed volume in the three directions *x*, *y*, *z*, were in the range 2–6% (see Table 2). These high values explain the differences observed between the surface fractions deduced from 2D analysis and those calculated from the 3D reconstruction.

Fig. 4(b) presents typical SEM "charged images" for each sample recorded with the inlens detector. For NiO ratios equal to 45 and 51% corresponding to Ni solid volume ratios of 23 and 25% (samples A1 and A2), all the Ni particles appeared dark, indicating that none of them participated in electrical conduction. For higher NiO ratios of 54, 56 and 61% (samples A3, A4 and A5), a majority of the Ni particles appeared bright, suggesting that they were percolated and conducting.

The combination between the two kinds of images ("Z-contrast" and "charge" images) rendered it possible to obtain the percolated Ni and non-percolated Ni ratios. These treatments were applied on at least five images for each sample and the results are presented in Table 4 and in Fig. 4(a) for comparison with the FIB-SEM tomography analysis. As the NiO wt.% fraction jumped from 51 to 54, the corresponding Ni particles suddenly percolated, suggesting that an anode with these ratios became an electronic conductor. For values of NiO wt.% between 51 and 54, the fraction of percolating Ni particles varied from 0 to more than 79%. This signifies that the initial NiO concentration must be accurately chosen to optimize the Ni ratio in the anode. If the Ni ratio is too high, the agglomeration of the Ni particles can further lead to electrode degradation and if it is

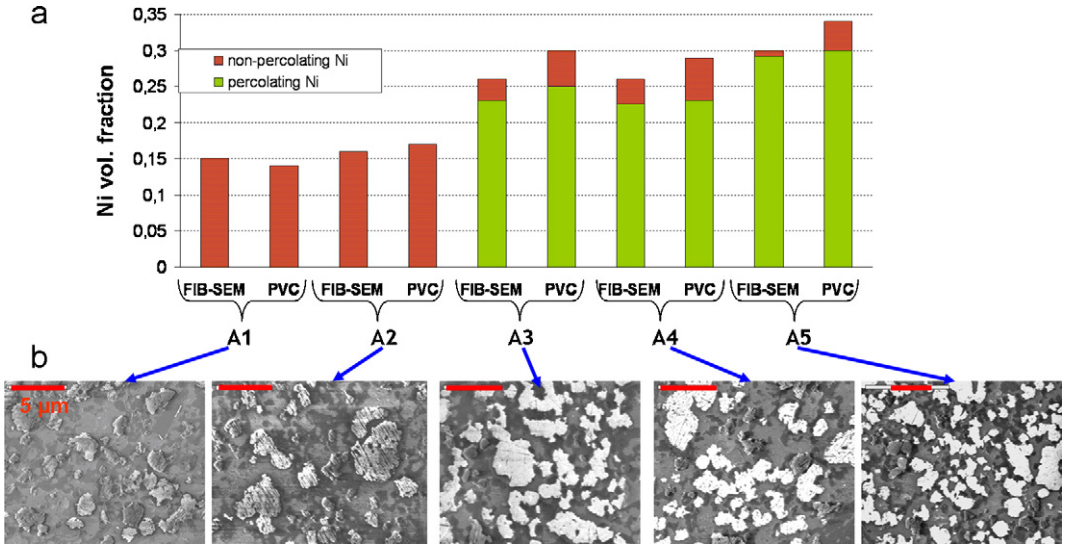

Fig. 4. (a) Percolating and non-percolating Ni fraction deduced from the FIB-SEM tomography and the PVC technique for the five samples. (b) Charge images recorded with the inlens SE detector: for samples A1 and A2, the Ni phase is not percolated (dark), while for samples A3 to A5, it is almost totally percolated (bright). The red-scale-bar in each image corresponds to 5 µm. (For interpretation of the references to color in this figure legend, the reader is referred to the web version of the article.)

too small the electronic conductivity can be too low or even equal to zero.

These results are in good accordance with those obtained by FIB-SEM tomography, which also pointed at a percolation threshold of the Ni particles for an initial NiO weight percentage between 51 and 54, corresponding in the FIB-SEM 3D images to Ni vol.% values comprised between 16 and 26%. This result agrees very well with the literature, since it has been established that if the Ni volume fraction in the cermet (Ni-8YSZ) is below 16%, the Ni clusters are systematically isolated from one another and cannot sinter together to form a percolating network [32].

3.2. Electrical and ionic conductivities

Experimental four-point electrical conductivity measurements were performed at room temperature (RT) on the anode surface for the five samples. Samples A1 and A2 gave conductivities too low to be measured while samples A3, A4 and A5 led to values of 337, 298 and 573 S cm^{-1}, respectively. As presented in our previous work [24], the effective electronic conductivity can be estimated through the resolution of the diffusive transport equation by using elemental conductivities taken from the literature (Table 3). For the samples A1 and A2 – since the Ni particles were not percolated, and the electronic conductivity of 8YSZ and of the gas diffusing in the pores was very small (see Table 3) – the effective electronic conductivity was negligible (<10^{-1} S cm^{-1}).

The results obtained for the samples A3, A4 and A5 are given in Table 5. One should notice that the experimental values were one order of magnitude smaller than the calculated effective electrical conductivities. These differences can be explained on the one hand by the experimental difficulties when it comes to creating good physical contacts between the four probes and the anode surface, which leads to a additional electrode-sample interface resistance [33], and on the other hand, the chosen Ni electrical conductivity value (1.5×10^5 S cm^{-1} at RT, see Table 3) used for the effective electrical conductivity calculation being debatable.

Indeed, Marinsek et al. [7] investigated the electrical properties of a series of Ni-YSZ cermets with different Ni volume fractions (from 0 to 100%). For the 100 vol.% Ni sample, the experimental electronic conductivity was close to 190 S cm^{-1} at 1123 K and therefore one order of magnitude smaller than the 10^4 S cm^{-1} value generally reported in the literature for Ni at this temperature (see Table 3). These large discrepancies can originate from the differences of microstructure between the Ni used here as reference and the real Ni inside the electrode.

For the samples A3, A4 and A5, the effective electronic conductivities $\sigma_{electronic}$, increased with the Ni concentration and appeared highly anisotropic. Since the direction of the anisotropy was not the same in the three samples, it was no easy task to make correlations with the preparation process. The volume fraction as determined in Section 3.1 was an important factor for explaining the increase in electrical conductivity between A3, A4 and A5 but a significant local variation was crucial and could physically correspond to an electrical resistance. In order to interpret the observed anisotropy in terms of microstructural considerations, the distribution of the percolated Ni inside the volume particles was considered. Fig. 5 displays the variation of the Ni surface fraction on each slice, separated by the voxel size (10 nm), in the three directions (*X*, *Y*, *Z*) for the three considered samples. Indeed, for distributions exhibiting a saw-edged behavior, the corresponding $\sigma_{electronic}$ was always smaller than the ones calculated in the other directions. In sample A3, the oscillations of the curves were the most marked for the *X* direction. As a result, the $\sigma_{electronic}$ value was the lowest compared with its counterparts in the *Y* and *Z* directions. Based on the same assumption, $\sigma_{electronic}$ was the lowest in the *Z* direction for A4 and in the *Y* direction for A5. Consequently, not only the Ni volume fraction plays an important role in the electrical behavior, but also the local Ni distribution.

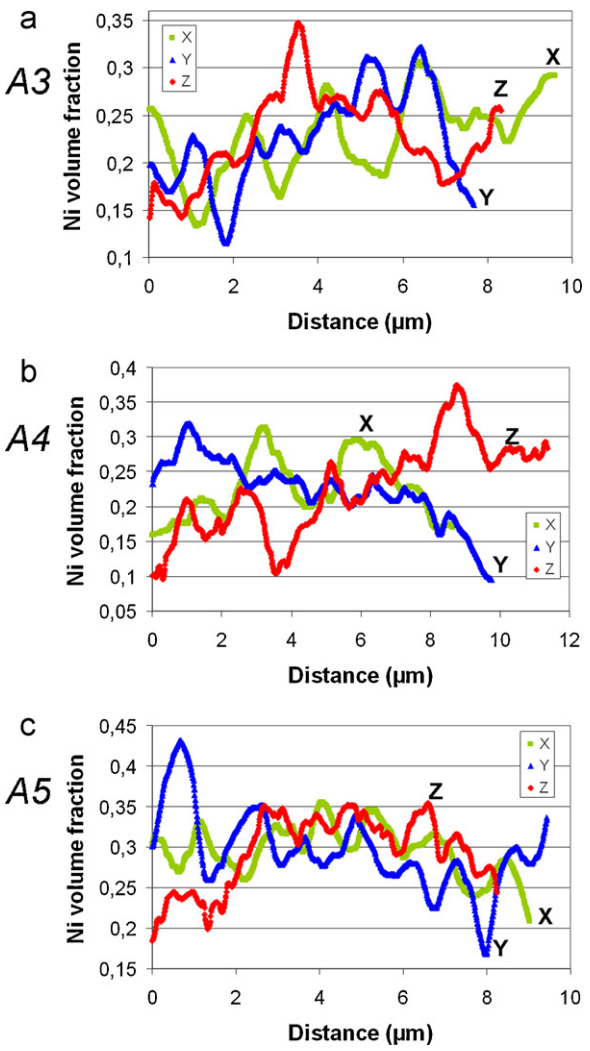

Fig. 5. Ni volume ratio in the *X*, *Y* and *Z* directions for sample A3 (a) A4 (b) and A5 (c). These graphs give information not only on the "absolute" Ni volume fraction value but also on its local variation. The distributions exhibiting a saw-edged behavior (A3–*X*; A4–*Y*; A5–*Z*) lead systematically to a lower $\sigma_{electronic}$ value.

The directional tortuosity of the Ni phase (τ_{Ni}) could be deduced from the calculated effective electronic conductivity ($\sigma_{electronic}$), the Ni volume fraction (ε_{Ni}) and the elemental electrical conductivity of Ni ($\sigma_{electronicNi}$, see Table 3) through the following equation:

$$\tau_{Ni} = \sqrt{\varepsilon_{Ni} \frac{\sigma_{electronicNi}}{\sigma_{electronic}}} \quad (1)$$

As a result, the large anisotropy in the Ni tortuosity values was correlated with the anisotropy in $\sigma_{electronic}$ (Table 5). Moreover, the tortuosity of the Ni particles decreased (in the order from 6 to 2) as the Ni volume fraction increased. This decrease of the tortuosity as a function of the volume fraction was a general tendency, which has yet to be reported in the literature regardless of the studied phase (pores, 8YSZ, Ni) [14,34].

From Fig. 6, it is obvious that in the samples studied here, the percolation threshold was shifted to the lowest Ni volume fraction values compared to the well know "33.33%" predicted by the EMPT. According to this theory, the electrical conductivity depended only on the volume fraction of the electrical conducting phase. More recently, Wu and Liu [6] developed a resistor network approach which only differed from the former by attempting to take into

Table 5
Effective electronic conductivities at 1123 K and RT for the samples A3, A4 and A5. The tortuosity of the Ni phase was deduced from the effective electronic conductivity values (see Eq. (1)).

Sample	A3			A4			A5		
Direction	*X*	*Y*	*Z*	*X*	*Y*	*Z*	*X*	*Y*	*Z*
$\sigma_{electronic}$ (S cm^{-1}) at 1123 K	124	209	296	281	252	66	561	378	473
$\sigma_{electronic}$ (S cm^{-1}) at RT	1786	3010	4262	4046	3629	950	8078	5443	6811
Tortuosity Ni	4.58	3.53	2.97	3.04	3.18	6.24	2.31	2.82	2.52

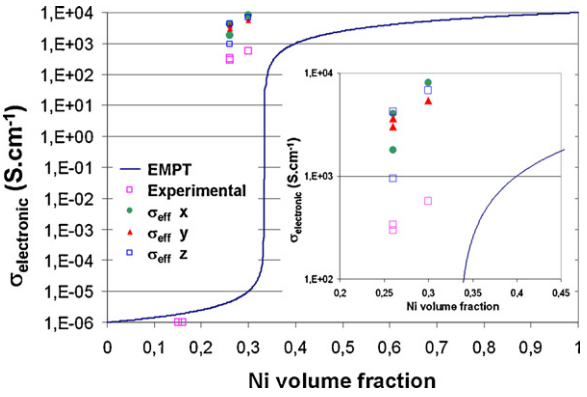

Fig. 6. Experimental and effective electronic conductivity at RT as a function of the Ni volume fraction. The relative positions of the corresponding symbols are highlighted in the inset of the figure. Since the electrical conductivity of the samples A1 and A2 were too small to be measured, they were fixed to 10^{-6} S cm^{-1} allowing the visualization of the experimental percolation threshold. The solid line represents the prediction of the EMPT, with its well-known percolation threshold at 1/3.

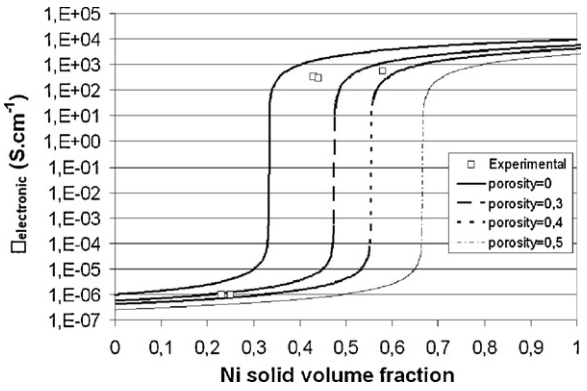

Fig. 7. Electronic conductivity as a function of the volume fraction of solid Ni predicted by the resistor network approach (Wu and Liu [6]) for various porosities. The squares correspond to the experimental electronic conductivity measured at RT. Since the electrical conductivity of the samples A1 and A2 were too small to be measured, they were fixed to 10^{-6} S cm^{-1} allowing the visualization of the experimental percolation threshold.

account the effect of porosity on the continuity of the conducting phase. The composite formed of Ni, 8YSZ and pores can be considered as a three-dimensional array of electrical resistors regardless of the shape and size of particles but assuming that the phases are randomly and evenly distributed throughout the composite. The electrical conductivities, as predicted by this model, are plotted as a function of the solid in Fig. 7 for various porosity fractions: 0, 0.3, 0.4 and 0.5. Without any porosity, the evolution of the electrical conductivity as a function of the volume fraction of solid Ni was similar to the one obtained by the EMPT. For larger porosity fractions, the percolation threshold displayed a shift towards higher volume fractions of solid Ni and was equal to ((1/3)/1 − porosity).

For the samples studied here, since the pore volume fractions were close to 35–40%, the expected value for the Ni percolation threshold was somewhere in the vicinity of 50% regarding the volume fraction of solid Ni (Fig. 7). According to the FIB-SEM experiments, the percolation threshold should be lower than 43% for this volume fraction. Usually, when preparing SOFC cells, one should consider that the initial NiO volume fraction must lead, after reduction, to a Ni solid volume fraction higher than 33.3% when mixing with YSZ. However, Kishimoto et al. have reported that a 50% Ni solid volume fraction in a Ni-8YSZ cermet did not lead to a percolated Ni network [20]. This was due to a relatively low Ni volume fraction in the final electrode; close to 25% because of a very large porosity (about 50%). According to our study, it appeared that the expected Ni solid volume fraction was insufficient for determining the percolation threshold and that the porosity ratio, not easily predictable when mixing the initial solid powders, must be approximately known.

The effective ionic conductivity decreased from about 4×10^{-3} S cm^{-1} (sample A1, 45 wt.% of NiO or 23% of Ni solid volume fraction) to 4×10^{-4} S cm^{-1} (sample A5, 61 wt.% of NiO or 58% of Ni solid volume fraction). In fact, the effective ionic conductivity varied almost linearly with the 8YSZ content. Moreover, as the σ_{ionic} was quite isotropic, the distribution of the 8YSZ particles was likely homogeneous.

3.3. Specific surface area and measurement of TPB_L

Regardless of the sample, the SSA of each phase was found to be independent of the initial composition. The values were systematically in the range 2–5 $\mu m^2\ \mu m^{-3}$: 3–4 $\mu m^2\ \mu m^{-3}$ for the porous phase, 3–5 $\mu m^2\ \mu m^{-3}$ for the 8YSZ phase and about 2 $\mu m^2\ \mu m^{-3}$ for the Ni phase (Table 6). These results are similar to those reported

Table 6
Specific surface and interface areas (SSA and SIA respectively) and surface-to-volume ratio (SVR) of each sample.

Samples		A1	A2	A3	A4	A5
SSA ($\mu m^2\ \mu m^{-3}$)	Pores	4.59	4.37	3.77	4.21	3.64
	8YSZ	5.21	4.45	3.62	4.37	3.07
	Ni	1.87	2.07	2.02	2.85	2.41
SIA ($\mu m^2\ \mu m^{-3}$)	Pores-8YSZ	3.97	3.37	2.69	2.87	2.15
	Pores-Ni	0.62	1.00	1.08	1.35	1.50
	YSZ-Ni	1.24	1.07	0.93	1.50	0.92
SVR ($\mu m^2\ \mu m^{-3}$)	Pores	13.11	12.14	9.67	10.27	7.58
	8YSZ	10.42	9.27	10.34	13.24	13.95
	Ni	12.47	12.94	7.77	10.96	8.03

Table 7
Total and active TPB_L of each sample.

Sample	A1	A2	A3	A4	A5
Total TPB_L ($\mu m\,\mu m^{-3}$)	8.8	9.3	7.5	11.2	7.2
Active TPB_L ($\mu m\,\mu m^{-3}$)	0	0	4.4	7.4	5.3
Active TPB (%)	0	0	58.5	66.1	73.5

by other authors [14,20]. The SIA – as defined in Section 2.3 – between the Ni particles and the pores had a tendency to increase with the starting NiO wt.% (from sample A1 to A5), indicating that more and more of the Ni surface was in contact with the pores. This increase can benefit the electrochemical reaction yields between the fuel and the Ni phase, but could also induce an unexpected Ni oxidation (into NiO) in the presence of hot water or oxygen. When going from sample A1 to A5, the SVR of the 8YSZ phase slightly increased while that of the porous and Ni phases was significantly reduced. For the Ni phase, a lowering occurred between sample A2 and A3, corresponding to the percolation threshold of the Ni particles. This was due to the fact that isolated clusters have larger surface-to-volume ratios than percolated clusters.

The total TPB_L results were in the range 7–11 $\mu m\,\mu m^{-3}$ with no significant variation as a function of the Ni content (Table 7). These values were close to those reported in the literature when the same calculation method was used [10–12,17]. For the samples A1 and A2, since the Ni particles were not percolated, the TPB were always inactive according to the definition given in Section 2.3. In the other samples, at least 58% of the TPB were active, with active TPB_L values of 4.4, 7.4 and 5.3 $\mu m\,\mu m^{-3}$ for samples A3, A4 and A5, respectively (Fig. 8).

The maximal TPB_L was obtained for sample A4. Wilson et al. [14] also reported results on TPB characteristics for Ni-8YSZ anodes with various weight percentages of initial NiO, i.e., 40, 50, 60 and 70 wt.%, using FIB-SEM tomography. In their work, the active TPB_L increased between 40 and 50 NiO wt.%, while it decreased for higher weight percentages. The maximal TPB_L was obtained for 50 wt.% NiO. These results are close to our observations since an optimal initial fraction of NiO powder was pointed out in both cases. However, a slight difference between the optimal values existed since the optimal NiO wt.% for the present study was close to 56. For higher NiO percentages, the number of active TPB decreased as also observed in the work of Wilson et al. [14] in calculations based on packing of spherical particles [35–37].

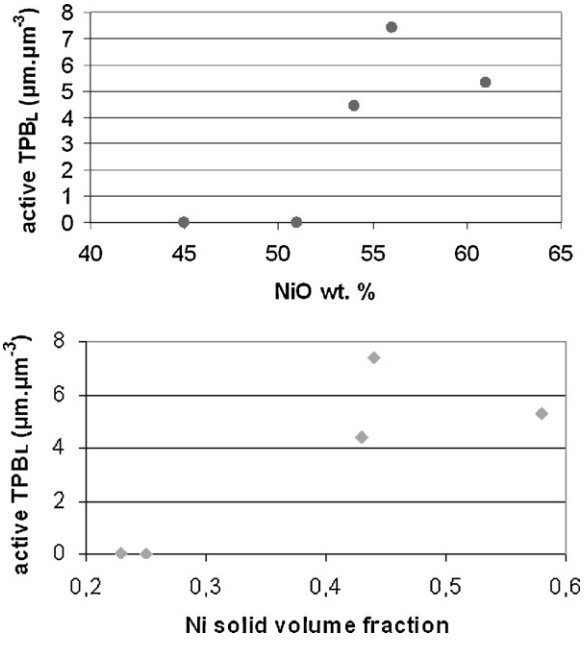

Fig. 8. Active TPB_L as a function of the NiO wt. fraction and Ni solid volume fraction.

4. Conclusions

This work has focused on the 3D analysis of a series of Ni-8YSZ SOFC anodes with various compositions of NiO, ranging from 45 to 61 wt.%. Microstructural parameters (volume fraction, connectivity), interfacial features (specific surface and interface areas and TPB_L) and effective transport properties (mainly electronic since the variation of Ni is addressed in this study) have been deduced from the analysis of the 3D reconstructions of the samples obtained by FIB-SEM tomography. A sudden rise in electrical conductivity, observed between 16 and 26 Ni vol.%, was correlated to a percolation threshold of the Ni particles. The PVC technique confirmed these results since the difference with the analysis arising from FIB-SEM were small. Moreover, it is not very time-consuming for sample preparation and treatment, and thus constitutes a powerful technique to verify the electrical conductivity or to observe the modifications induced by aging or redox cycles. The present study confirms that the percolation of the Ni particles could not occur for Ni volume fractions smaller than 16%. However, the comparison of our results with other reports demonstrated that both the volume fraction of solid Ni and the porosity were decisive on the percolation threshold value.

The determination of the surface and interface features suggests that the Ni specific surface area increased with the NiO wt. fraction and was mostly in contact with the pores rather than with the 8YSZ particles. This increase can benefit the electrochemical reaction yields between the fuel and the Ni phase, but could also induce an unexpected Ni oxidation (in NiO) in the presence of hot water or oxygen. The maximum active TPB_L was obtained for the sample characterized by a volume fraction of solid Ni of about 44%. Even if this value is in good accordance with those published in the literature (40–50%), it cannot be considered as a universal value since the optimal active TPB_L depends not only on the composition but also on the microstructure of the electrode (which may differ as a result of fabrication precursors and processes).

Acknowledgments

The authors would like to thank J. Vulliet for the electrical conductivity measurements and T. Piquero for the samples fabrication.

References

[1] S. Singhal, K. Kendall, High-Temperature Solid Oxide Fuel Cells: Fundamentals, Design and Applications, Elsevier Advanced Technology, Oxford, UK, 2003.
[2] W.Z. Zhu, S.C. Deevi, Mater. Sci. Eng. A 362 (2003) 228–239.
[3] M. Mori, T. Yamamoto, H. Itoh, H. Inaba, T. Tagawa, J. Electrochem. Soc. 145 (1988) 1374–1381.
[4] D.S. Simwonis, F. Tietz, D. Stover, Solid State Ionics 132 (2000) 241–251.
[5] N.Q. Minh, J. Am. Ceram. Soc. 76 (1993) 563–588.
[6] Z. Wu, M. Liu, Solid State Ionics 93 (1997) 65–84.
[7] M. Marinsek, A. Pejovnik, J. Macek, J. Eur. Ceram. Soc. 27 (2007) 959–964.
[8] R. Landauer, J. Appl. Phys. 23 (1952) 779–784.
[9] H.S. Hong, U.S. Chae, S.T. Choo, J. Alloys Compd. 449 (2008) 331–334.
[10] J.R. Wilson, W. Kobsiriphat, R. Mendoza, H.-Y. Chen, J.M. Hiller, D.J. Miller, K. Thornton, P.W. Voorhees, S.B. Alder, S.A. Barnett, Nat. Mater. 5 (2006) 541–544.
[11] J.R. Wilson, S.A. Barnett, Electrochem. Solid-State Lett. 11 (10) (2008) B181–B185.
[12] J.R. Wilson, M. Gameiro, K. Mischaikow, W. Kalies, P.W. Voorhees, S.A. Barnett, Microsc. Microanal. 15 (2009) 71–77.
[13] S.A. Barnett, J.R. Wilson, W. Kobsiriphat, H.-Y. Chen, R. Mendoza, J.M. Hiller, D.J. Miller, K. Thornton, P.W. Voorhees, S.B. Alder, Microsc. Microanal. 13 (2007) 596–597.
[14] J.R. Wilson, J.S. Cronin, S.A. Barnett, Scripta Mater., doi:10.1016/j.scriptamat.2010.09.025.
[15] J.S. Cronin, J.R. Wilson, S.A. Barnett, J. Power Sources 196 (2011) 2640–2643.

[16] J.R. Smith, A. Chen, D. Gostovic, D. Hickey, D. Kundiger, K.L. Duncan, R.T. DeHoff, K.S. Jones, E.D. Washman, Solid State Ionics 180 (2009) 90–98.
[17] P.R. Shearing, Q. Cai, J.I. Golbert, V. Yufit, C.S. Adjiman, N.P. Brandon, J. Power Sources 195 (2010) 4804–4810.
[18] H. Iwai, N. Shikazono, T. Matsui, H. Teshima, M. Kishimoto, R. Kishida, D. Hayashi, K. Matsuzaki, D. Kanno, M. Saito, H. Muroyama, K. Eguchi, N. Kasagi, H. Yoshida, J. Power Sources 195 (2010) 955–961.
[19] K. Matsuzaki, N. Shikazono, N. Kasagi, J. Power Sources 196 (2011) 3073–3082.
[20] M. Kishimoto, H. Iwai, M. Saito, H. Yoshida, J. Power Sources (2011), doi:10.1016/j.jpowsour.2010.12.100.
[21] J. Joos, T. Carraro, A. Weber, E. Ivers-Tiffee, J. Power Sources, doi:10.1016/j.jpowsour.2010.10.006.
[22] L. Holzer, B. Munch, B. Iwanschitz, M. Cantoni, T. Hocker, Th. Graule, J. Power Sources, doi:10.1016/j.jpowsour.2010.08.006.
[23] L. Holzer, B. Iwanschitz, T. Hocker, B. Munch, M. Prestat, D. Wiedemann, U. Vogt, P. Holtappels, J. Sfeir, A. Mai, Th. Graule, J. Power Sources 196 (2011) 1279–1294.
[24] N. Vivet, S. Chupin, E. Estrade, T. Piquero, P.L. Pommier, D. Rochais, E. Bruneton, J. Power Sources, doi:10.1016/j.jpowsour.2011.03.060.
[25] K. Thyden, Y.L. Liu, J.B. Bilde-Sorensen, Solid State Ionics 178 (2008) 1984–1989.
[26] P. Hovington, D. Drouin, R. Gauvin, Scanning 19 (1997) 1–14.
[27] http://www.vsg3d.com.
[28] A.S. Joshi, K.N. Grew, J.R. Izzo Jr., A.A. Perachio, W.K.S. Chiu, J. Fuel Cell Sci. Technol. 7 (2010) 011006.
[29] L. Shen, Z. Chen, Chem. Eng. Sci. 62 (2007) 3748–3755.
[30] T.G. Sherwood, R.L. Pigford, C.R. Wilke, in: B.J. Clark, J.W. Maisel (Eds.), Mass Transfer, McGraw-Hill Inc., New York, 1975, pp. 39–43.
[31] J. Sanyal, G.M. Goldin, H. Zhu, R.J. Kee, J. Power Sources 195 (2010) 6671–6679.
[32] R.M.C. Clemmer, S.F. Corbin, Solid State Ionics 180 (2009) 721–730.
[33] E.J. Zimmey, G.H.B. Dommett, R.S. Ruoff, D.A. Dikin, Meas. Sci. Technol. 18 (2007) 2067–2073.
[34] J.R. Wilson, J.S. Cronin, A. Duong, S. Rukes, H-Yi. Chen, K. Thornton, D. Mumm, S. Barnett, J. Power Sources 195 (2010) 1829–1840.
[35] C. Metcalfe, O. Kesler, T. Rivard, F. Gitzhofer, N. Abatzoglou, ECS Trans. 25 (2) (2009) 1185–1194.
[36] C. Metcalfe, O. Kesler, T. Rivard, F. Gitzhofer, N. Abatzoglou, J. Electrochem. Soc. 157 (9) (2010) B1326–B1335.
[37] B. Kenney, M. Valmanis, C. Baker, J.G. Pharoah, K. Karan, J. Power Sources 189 (2009) 1051–1059.